Journal of Materials Research and Technology 39 (2025) 6156–6168

Contents lists available at ScienceDirect

Journal of Materials Research and Technology

journal homepage: www.elsevier.com/locate/jmrt

Wear and corrosion performance of textured Hastelloy-X fabricated by laser powder bed fusion: Process window and microstructural features

Sung-Hyun Park [a,b], Fatmanur Ayten [c], Asli Gunay Bulutsuz [c,*], Ozkan Gokcekaya [a,b,**], Muhammed Enes İlgazi [d], Hakan Yilmazer [e], Burak Dikici [f], Takayoshi Nakano [a,b,***]

[a] Division of Materials and Manufacturing Science, Graduate School of Engineering, The University of Osaka, 2-1, Yamadaoka, Suita, Osaka, 565-0871, Japan
[b] Anisotropic Design & Additive Manufacturing Research Center, The University of Osaka, 2-1, Yamadaoka, Suita, Osaka, 565-0871, Japan
[c] Department of Mechanical Engineering, Yildiz Technical University, Besiktas, Istanbul, Turkey
[d] Department of Aircraft Maintenance and Repair, School of Civil Aviation, Istanbul Nisantasi University, Istanbul, Turkey
[e] Department of Metallurgical and Materials Engineering, Yildiz Technical University, 34220, İstanbul, Turkey
[f] Department of Mechanical Engineering, Ataturk University, Erzurum, 25240, Turkey

ARTICLE INFO

Keywords:
Hastelloy-X
Laser powder bed fusion
Densification
Crystallographic texture
Wear performance
Corrosion resistance

ABSTRACT

This study investigated the effect of volumetric energy density (VED) on the densification and microstructural evolution of Hastelloy-X (HX) alloy fabricated by the laser powder bed fusion (L-PBF) process, and how these changes affect wear and corrosion performance. Variations in VED altered melt pool geometries, which influenced densification. In addition, VED also affected the growth direction of <100> cellular microstructures, resulting in different crystallographic texture development. Specifically, high VED showed the lowest densification with strong <100> alignment in x,y, and z directions. Meanwhile, medium VED exhibited the highest densification with a mixed <100> and <110> crystallographic texture along the building direction, while low VED led to moderate densification with weak <100> alignment overall. The wear and corrosion properties of the samples varied with their densification and microstructural characteristics. In terms of wear mechanisms, a distinct load dependence was observed. Oxidative wear dominated at low loads, where the strong (100)-oriented crystallographic texture promoted oxide stability and improved the wear resistance. While deformation wear prevailed at higher loads, where hardness became the determining factor. As for corrosion resistance, higher densification, grain refinement, and high dislocation density generally facilitated passive film formation and improved resistance. However, crystallographic texture should also be considered, since (100)-oriented regions are more prone to corrosion than other orientations, indicating that the crystallographic texture inherent to L-PBF processing is an important factor in corrosion behavior. The results demonstrate that optimizing L-PBF process parameters is essential for tailoring microstructure and improving the wear and corrosion resistance of Ni-based superalloys.

1. Introduction

Ni-based superalloys are key materials across various high-demand industries, including aerospace, marine, and nuclear applications, due to their superior mechanical performance and environmental degradation resistance [1–4]. In particular, Hastelloy-X (HX) is a solid solution-strengthened Ni-based superalloy that exhibits excellent mechanical strength at both room and elevated temperatures and good oxidation resistance, thereby enabling its widespread use as a structural material in current-generation aerospace and nuclear components [5–7]. However, the conventional casting process becomes costly and time-consuming owing to the complex and highly precise geometry of components required in service environments. In this case, additive manufacturing (AM), an emerging technology based on the

* Corresponding author. Department of Mechanical Engineering, Yildiz Technical University, Besiktas, Istanbul, Turkey.
** Corresponding author. Division of Materials and Manufacturing Science, Graduate School of Engineering, The University of Osaka, 2-1, Yamadaoka, Suita, Osaka, 565-0871, Japan.
*** Corresponding author. Division of Materials and Manufacturing Science, Graduate School of Engineering, The University of Osaka, 2-1, Yamadaoka, Suita, Osaka, 565-0871, Japan.
E-mail addresses: gunay@yildiz.edu.tr (A.G. Bulutsuz), ozkan@mat.eng.osaka-u.ac.jp (O. Gokcekaya), nakano@mat.eng.osaka-u.ac.jp (T. Nakano).

https://doi.org/10.1016/j.jmrt.2025.10.229
Received 16 July 2025; Received in revised form 27 September 2025; Accepted 27 October 2025
Available online 31 October 2025

layer-by-layer deposition of materials, offers significant advantages such as simplified post-processing, improved spatial distribution, and the capability to design compositional and microstructural features [8,9].

AM processes can be categorized into several types depending on the feed system and energy source [10]. Among them, the laser powder bed fusion (L-PBF) process, the most widely adopted technique, utilizes a smaller beam size and finer powder particles, resulting in enhanced processing accuracy, higher geometrical resolution, and improved surface quality [11]. Given these advantages, extensive research has been conducted on various alloy systems, such as Ti- [12], Al- [13], high-entropy- [14] and Cu- [15] based alloys, as well as intermetallic compounds [16], demonstrating the suitability of L-PBF for high-performance applications, particularly due to its ability to achieve significantly improved properties compared with conventional manufacturing methods [14,17]. HX has also been considered a promising candidate for the L-PBF process. Iveković A et al. [18] aimed to reduce cooling rates and suppress micro-cracks during the L-PBF of HX samples through adjustments in hatch spacing and laser beam profile. As a result, they successfully produced crack-free samples, which exhibited superior mechanical properties compared to conventionally manufactured counterparts. In addition, Han Q et al. [19] achieved both crack-free and further enhanced mechanical properties compared to L-PBF of HX parts by introducing 1 wt.% titanium carbide nanoparticles and promoting the heterogeneous microstructure. Agrawal S et al. [20] and Yin Y et al. [21] investigated the evolution of microstructure and mechanical properties in L-PBF fabricated HX through various post-heat treatment conditions, in order to clarify the effects of heat treatments on phase transformation and mechanical property optimization.

On the other hand, steep thermal gradients typically established in the L-PBF process guide grain growth along the direction of maximum heat flow. This condition favors the grain alignment with the preferred crystal direction parallel to the thermal gradient, leading to the formation of elongated columnar grains. In addition, these grains are sustained through epitaxial growth across successive layers. The overall crystallographic texture evolution is governed by the interplay between the thermal gradient direction and the epitaxial growth tendency [22,23]. The development of crystallographic texture can be tailored by manipulating process parameters such as the scan strategy [12,24], energy density (adjusted via laser power, scanning speed, etc.) [25,26], and substrate preheating [27]. These process parameters induce variations in crystallographic texture, which have been reported to significantly affect the deformation behavior of HX fabricated by the L-PBF process. Hibino et al. [28] observed distinct crystallographic textures in L-PBF fabricated HX: (1) a single crystalline-like structure with <100> orientation along the building direction, (2) a single crystalline-like structure with <110> orientation, (3) a crystallographic lamellar microstructure, and (4) a polycrystalline microstructure. These crystallographic variations influenced tensile properties, highlighting the role of crystallographic texture in optimizing the performance of HX components fabricated by the L-PBF process. Similarly, to investigate the effect of crystallographic texture, Sanchez-Mata et al. [29] demonstrated that the extracted sample orientation along the building direction led to different mechanical properties under identical processing conditions. Additional studies collectively emphasize that crystallographic texture development in the HX components via the L-PBF process has been predominantly explored with respect to mechanical properties [30,31].

However, the influence of crystallographic texture on functional properties such as wear and corrosion resistance has been insufficiently explored in HX. Although several studies have focused on the anisotropic functional behavior of HX fabricated by the L-PBF process [32,33], and crystallographic texture-related effects have been reported in other alloy systems [34,35], such comprehensive investigation for HX is still lacking. This gap highlights the necessity of evaluating whether crystallographic texture-driven effects on functional performance also exist in HX, particularly considering its application in aggressive service environments. The present study systematically investigates the influence of L-PBF process parameters on densification and microstructural evolution. Especially, emphasis is placed on examining how crystallographic texture correlates to functional properties, including tribological and corrosion behavior. By analyzing HX components fabricated under varying volumetric energy density (VED) conditions, the study aims to elucidate how process-induced microstructural changes govern functional degradation mechanisms, thereby contributing valuable insights for the design of durable, application-specific components for advanced applications.

2. Materials and methods

2.1. Sample fabrication

Fig. 1(a) shows the typical scanning electron microscopy (SEM) image of the gas-atomized HX powder utilized for this study. The powders have a spherical shape and the powder size distribution was determined as $D_{10} = 17.4$ μm, $D_{50} = 33.9$ μm, and $D_{90} = 63.1$ μm using a particle size analyzer (Fig. 1(b)). The detailed chemical composition of the alloy is included in Table 1. As shown in Fig. 1(c), samples with dimensions of 10 mm × 10 mm × 10 mm along the x, y, and z directions were fabricated using an L-PBF machine (EOS M290) equipped with a 400 W Yb-fiber laser as the primary heat source. Herein, the x and y directions are scanning directions, and the z direction is the building direction. The bidirectional scanning with a rotation of 90° between layers was applied, which is the so-called scan strategy XY [36]. The building platform has been heated to 80 °C to prevent unexpected temperature fluctuations from the laser input and to ensure consistency during the fabrication.

2.2. Phase and microstructure characterization

As shown in Fig. 1(d), the fabricated HX specimens were cut on the yz-plane representing the x direction by the wire electrical discharge machine. The cross sections of specimens were then prepared as a mirror polish surface quality using SiC paper and colloidal silica. An optical microscope (OM) and ImageJ software were used to assess the relative densities (relative density% = 100 % − defects density%). Phase analysis was carried out by X-ray diffraction (XRD) using Cu Kα radiation.

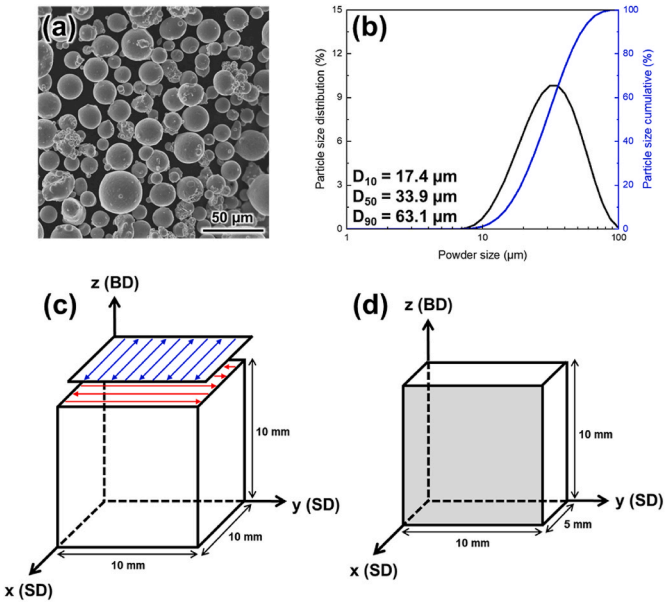

Fig. 1. (a) SEM image and (b) particle diameter distribution of HX powder. Schematic representation of (c) fabricated specimen dimensions with the scanning strategy applied and (d) the characterized plane.

Table 1
Elemental composition of HX raw powder (wt.%).

	Ni	Cr	Fe	Mo	W	Co	C	Si	Mn	B	O	N
Composition	Bal.	20.93	17.89	8.73	0.84	1.46	0.01	0.18	0.01	<0.003	0.019	0.009

The XRD data were obtained by point scanning in the 2θ angular range from 30° to 80° with a 0.02° step size and a 2 s scan time per step. Microstructural characteristics were investigated using a field emission SEM equipped with electron backscatter diffraction (EBSD) and energy-dispersive X-ray spectroscopy (EDS). The melt pool shape with cell elongation was determined after etching with an HF: HNO_3: H_2O = 35: 55: 100 solution at 50–60 °C for 60 min.

2.3. Mechanical property testing

Vickers hardness tests were performed in the yz-plane. Prior to the test, the mirror-polished surface quality was prepared in the same manner as previous densification and microstructure characterization to exclude the influence of surface roughness. The testing was conducted with a 1.961 N load applied for 15 s. In addition, hardness was measured at various locations across the sample surface to ensure representative values, and the results are presented as mean ± standard deviation.

2.4. Tribological characterization

Dry sliding friction tests were performed using a pin-on-disc machine (Model: Oscillating TRIB Otester) in the yz-plane. ASTM G99: a standard test method for wear testing with a pin-on-disk apparatus. The samples were mirror-polished prior to the tribological evaluation. The pin is positioned against the counterface of a rotating disc (Al_2O_3) with a wear track diameter of 2.0 mm. Loading of the pin against the disc is achieved through a deadweight loading system. Experiments are executed on all samples under standard loads of 2 N, 5 N, and 10 N loads with a sliding speed of 60.00 mm/s, spanning a total sliding distance of 100 m at room temperature. The illustrative depiction of the pin-on-disc tribometer can be seen in Fig. 2. Prior to and after each test, the samples and wear track are cleaned using acetone. For wear track characterization, a mechanical profilometer (Mahr MarSurf PS1) and an SEM with EDS were used for area measurements and wear mechanism analysis.

2.5. Electrochemical corrosion testing

The electrochemical corrosion evaluation of the L-PBFed HX samples was conducted in the yz-plane using a 3.5 wt% NaCl solution to simulate a saline environment at room temperature. The evaluation used a three-electrode electrochemical setup consisting of a graphite rod as the counter electrode, an Ag/AgCl (3 M KCl) electrode as the reference electrode, and the HX samples as the working electrode. Prior to the potentiodynamic scanning (PDS) tests, the open circuit potential (OCP) was monitored for approximately 2 h to allow the system to reach a stable equilibrium state. The PDS tests were then performed in both cathodic and anodic directions at a scanning rate of 1 mV s^{-1}. The polarization scan ranged from −0.3 V below the E_{ocp} value and continued in the anodic direction until the transpassive region was identified. Each electrochemical test was conducted at least three times to ensure reproducibility, with the variation in polarization curves among different samples determined to be ±10 mV.

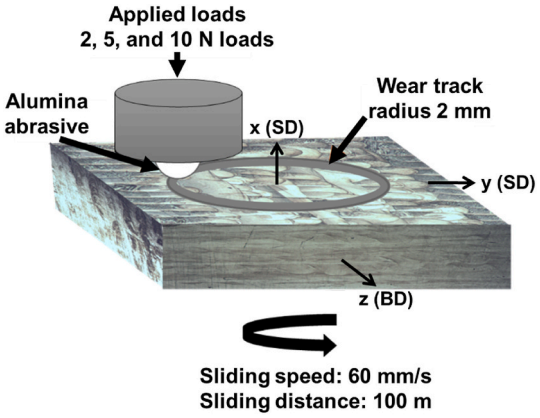

Fig. 2. Schematic representation of the wear test apparatus with experimental conditions.

3. Results

3.1. Processability and densification as a function of the L-PBF process parameters

Process maps of the surface morphology were first examined in order to optimize the fabrication conditions. The surface morphologies of the samples formed under different conditions were classified as wavy, fail, good, and porous types by observing their appearance. Here, the VED was calculated by the following equation:

$$\mathrm{VED} = \frac{P}{v \cdot d \cdot t} \quad (1)$$

Where P is the laser power, v is the scanning speed, d is the hatch spacing, and t is the layer thickness. Additionally, the different colors in red, green, and blue represent changes in d corresponding to 0.06 mm, 0.08 mm, and 0.10 mm, respectively.

As displayed in Fig. 3, predominantly wavy surfaces were observed when 0.06 mm of d (red) was applied, particularly at high v conditions where specimens failed to fabricate. Because the small hatch spacing increases thermal accumulation, reduces viscosity, and increases Marangoni flow [37]. Therefore, the intensified mass transfer to previous tracks causes micro-humping. In addition, the track became more unstable and irregular due to discontinuous droplets in high v conditions, which were demonstrated in previous studies [37,38]. This is a

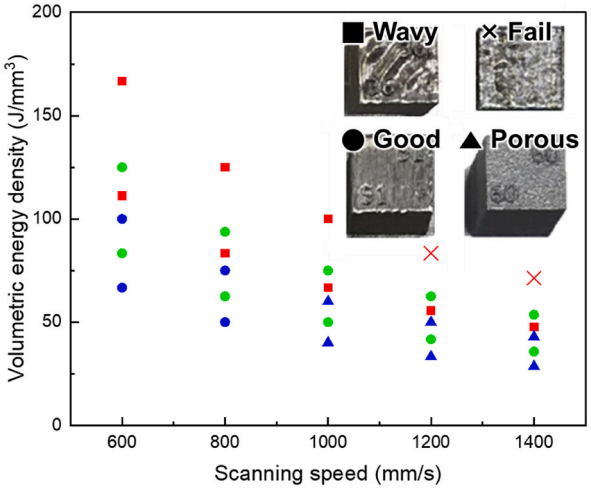

Fig. 3. Processability of the HX samples fabricated by the L-PBF process with varied volumetric energy density. Red, green, and blue exhibit d variations of 0.06 mm, 0.08 mm, and 0.10 mm, respectively.

phenomenon known as the balling phenomenon and can increase surface roughness, eventually leading to sample failure. On the other hand, due to the insufficient overlap between the laser tracks and/or unmelted powder trapped in irregularly shaped pores, the employment of 0.10 mm of *d* (blue) with high *v* conditions was represented as a porous surface. Therefore, the 0.08 mm of *d* (green) condition, which had an overall flat and compacted surface, was intensively observed.

As shown in Fig. 4, the general relative density of the fabricated HX samples as a function of the VED solely in the *d* 0.08 condition was investigated. An increasing tendency of the relative density can be found with increasing VED. High densification was observed in the VED range of 35–95 J/mm^3. However, further excessive VED input induces a decrease in densification. In order to study samples of VED conditions over a wide range, representative samples were collected for further investigation. Hereafter, the corresponding representative samples are referred to as HX1, HX2, and HX3, respectively. The detailed process parameters are listed in Table 2.

Fig. 4(a−c) shows the cross-sectional images taken by OM on the yz-plane representing the x direction of the fabricated HX samples with the variation of the VED input. Different from previous studies [18,19], the formation of the microcrack was not observed in all samples. Microcracking in Hastelloy-X samples made using the L-PBF process is mainly due to two factors [19,39]. Firstly, the partial dissolution of the carbide phases because of the abrupt heating and cooling in the L-PBF process forms a low melting point eutectic liquid film at grain boundaries. Secondly, the liquid film can act as low tensile-strength regions susceptible to thermal residual stress, thus, leading to the formation of microcracks. However, the carbon element in the HX powder used for this study was very low at 0.01 wt%, which suggests that the composition contributed to microcracking mitigation. Nevertheless, the measured relative density of the HX1 (red) sample was 98.39 ± 0.13 %, which is the lowest among the representative samples because it had typical keyhole pores. Meanwhile, the HX2 (green) and HX3 (blue) samples contained small gas pores and showed almost full densification with 99.96 ± 0.01 % and 99.88 ± 0.05 %, respectively. From the aforementioned detailed process parameters in Table 2, the employed *P*, *d*, and *t* during the L-PBF process were identical for the representative samples, only the *v* is gradually increased in steps of 400 mm/s. Therefore, the lower relative density of the HX1 sample can be considered the formation of the keyhole types of melt pool because the slower *v* results in excessively high VED input. While HX2 and HX3 samples were fabricated under the optimal range of VED inputs that ensure higher densification with the faster *v*. A similar phenomenon has been observed in L-PBFed titanium and superalloys [38,40].

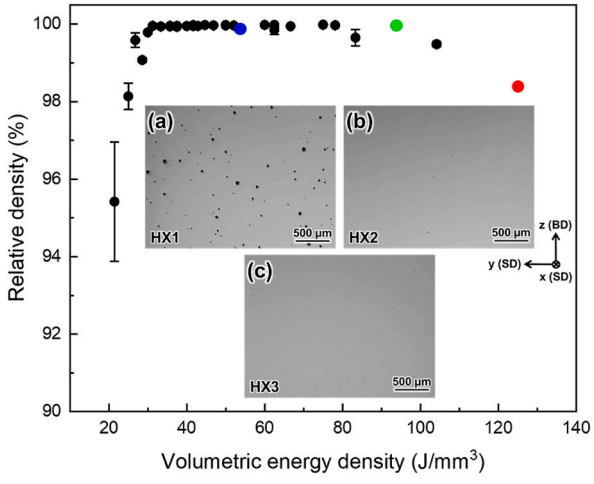

Fig. 4. Relative density−VED plots with inset OM images were taken from the HX samples fabricated by the L-PBF process in the yz-plane using (a) HX1 (red), (b) HX2 (green), and (c) HX3 (blue) specimens, respectively.

Table 2
The representative Hastelloy-X alloy samples have been produced by the laser powder bed fusion process with the corresponding abbreviation, detailed process parameters, and calculated volumetric energy density input.

Abbreviation	Scan strategy	*P* (W)	*v* (mm/s)	*d* (mm)	*h* (mm)	VED (J/mm^3)
HX1	XY	360	600	0.08	0.06	125
HX2	XY	360	1000	0.08	0.06	94
HX3	XY	360	1400	0.08	0.06	54

3.2. Characteristics of phase and microstructure

The normalized XRD patterns of the HX1, HX2, and HX3 are shown in Fig. 5. The peaks of (111), (200), and (220) indicate that all the samples only consist of γ-phase without any additional phases, indicating that different VED inputs have no effect on phase constitution of L-PBFed HX samples, which is in line with the previous observation [41]. However, the relative peak intensity of typical crystal planes varies with the VED inputs. In the case of the HX1 sample, the (200) peak was predominantly observed. Meanwhile, the relative intensity of the (200) peak was the highest in the HX2 and HX3 samples, while the (111) and (220) peaks were clearly distinguishable. Compared with the HX2 and HX3 samples, weak peak intensities for the (111) and (220) were observed in the HX3 sample. These results suggest that the crystallographic texture is dependent on the process parameters.

Therefore, a further detailed investigation of microstructure characteristics was carried out using SEM-EBSD. Fig. 6 presents the colorized inverse pole figure (IPF) maps according to the crystallographic texture in the yz-plane, and the corresponding {100} pole figures (PFs), high-angle grain boundaries (HAGBs, >15°), kernel average misorientation (KAM), and Taylor factor maps are presented. In the IPF maps (Fig. 6 (a1−c1)), the predominantly red color, which represents the (100) orientation was observed in the HX1 sample. However, the color of the HX2 sample was altered to a mixture of red and green, and the color of the HX3 sample turned mainly red again. The PFs provided further support for these results (Fig. 6(a2−c2)), the crystallographic texture of the HX1 sample gave rise to strong <100> alignments along the x,y, and z directions with the highest multiple of uniform density (MUD) as 22.12. Meanwhile, the HX2 sample revealed that the crystallographic texture was composed of <100> and/or <110> components along the z direction with slight deviation, and it exhibited a relatively high MUD value of 11.14 because of epitaxial growth tendencies. However, the <100> orientation along the x,y, and z directions stabilized again, with the lowest MUD value of 7.18 in the HX3 sample. In addition, strong crystallographic texture formation increases grain size because of the epitaxial growth, and it suggests that the crystal alignment of

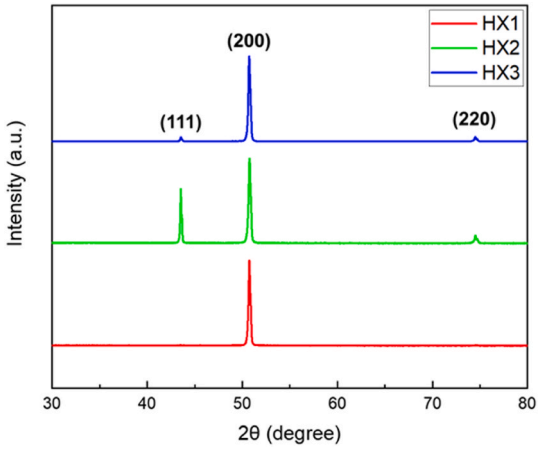

Fig. 5. XRD patterns of the HX1, HX2, and HX3 specimens.

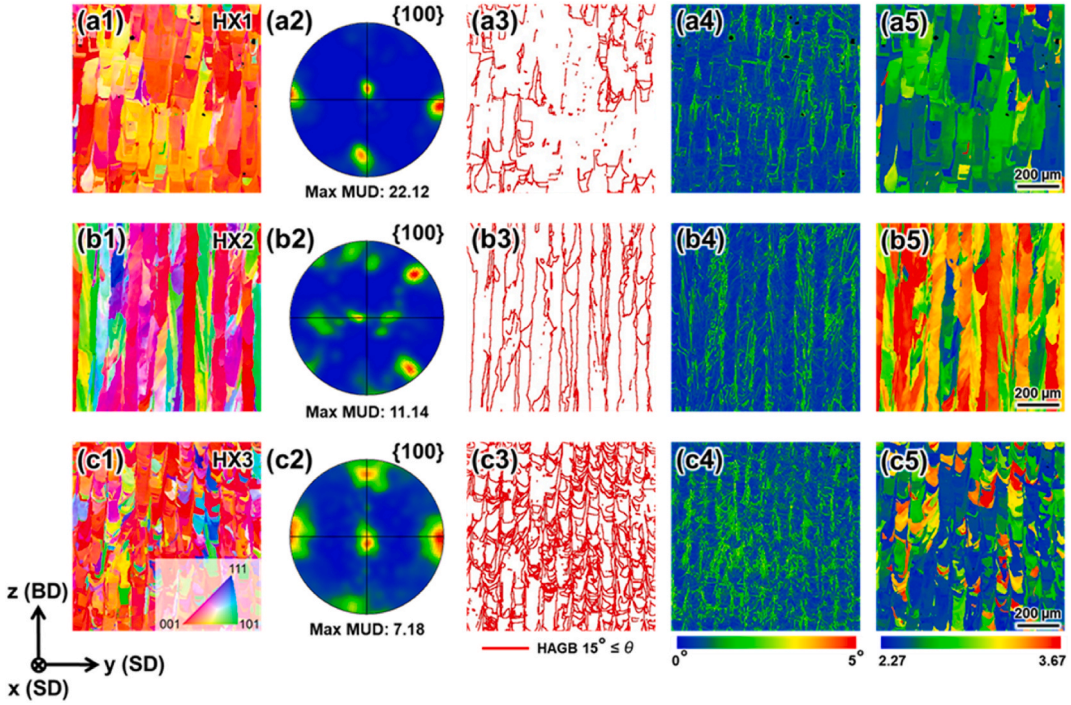

Fig. 6. For the HX1, HX2, and HX3 samples, obtained (a1−c1) IPF maps and (a2−c2) PFs in the yz-plane. The corresponding (a3−c3) HAGBs, (a4−c4) KAM, and (a5−c5) Taylor factor maps, respectively.

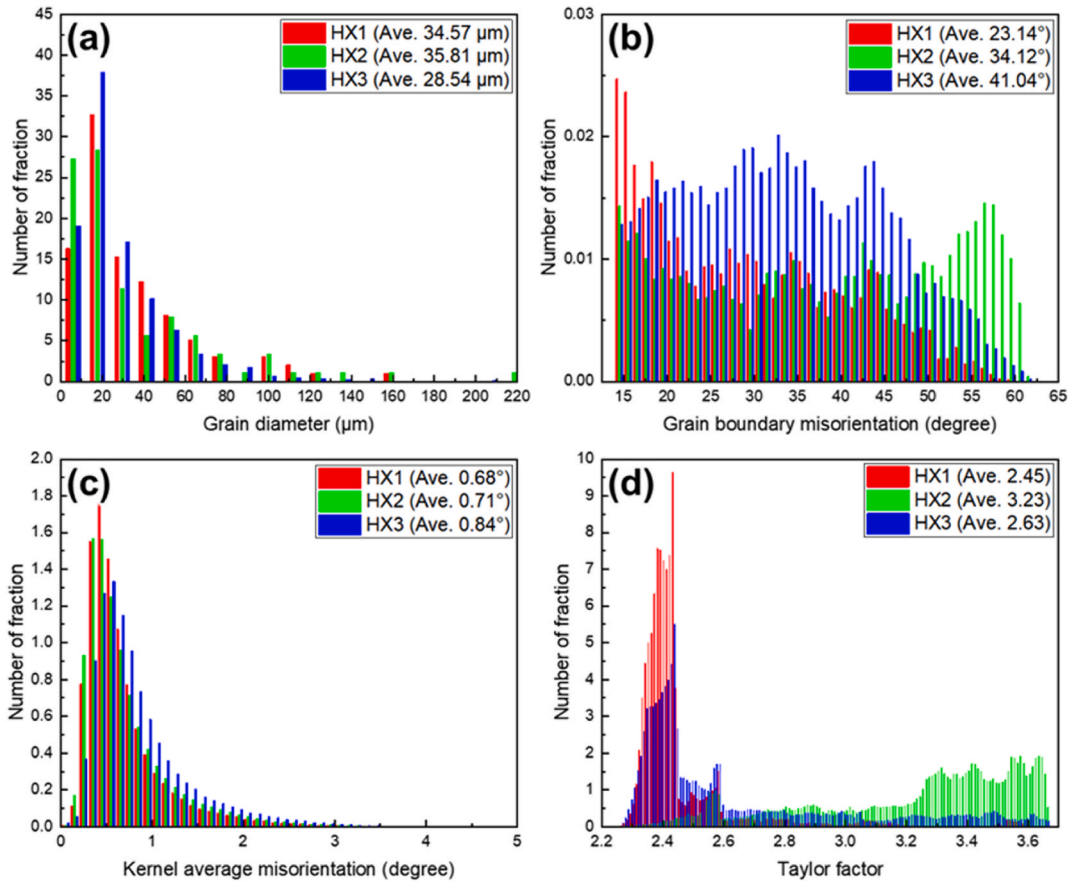

Fig. 7. (a) Grain size, (b) HAGBs, (c) KAM, and (d) Taylor factor distributions with the quantitative averages for HX1, HX2, and HX3 samples, respectively.

neighboring grains, results in a decrease in grain boundary misorientation [27]. Thus, the density of HAGBs (Fig. 6(a3−c3)) was low in the epitaxial growth area. In addition, KAM (Fig. 6(a4−c4)), representing the average misorientation between points on the grid and its neighbors also showed a similar distribution. However, the Taylor factor (Fig. 6 (a5−c5)), which predicts the yield response of grain as a function of stress and grain orientation [26,41], did not show apparent correlation. Among the representative samples, the HX1 sample showed the lowest Taylor factor, the HX2 sample was the highest, and the HX3 sample was intermediate.

Fig. 7 provides quantitative values along with histograms for understanding the microstructural characteristics for (a) grain size, (b) HAGBs, (c) KAM, and (d) Taylor factor. The development of a strong crystallographic texture usually allowed the grain to elongate and grow across the melt pool, as illustrated in Fig. 6. However, the HX2 sample represented more stable epitaxial growth along the z direction, although the HX1 sample showed higher MUD values compared to the HX2 sample. Therefore, the average grain size exhibited a slightly increasing and then decreasing tendency, from 34.57 μm in the HX1 to 35.81 μm in the HX2, and 28.54 μm in the HX3 samples (Fig. 7(a)). On the other hand, the average values of HAGBs and KAM showed an ascending order with the development of the weak crystallographic texture. The HX1 sample represented the lowest average HAGBs and KAM values of 23.14° and 0.68°, respectively. While the HX2 sample showed 34.12° and 0.71°, the HX3 sample had the highest values at 41.04° and 0.84° (Fig. 7(b) and (c)). In terms of the Taylor factor, the average values of the HX1, HX2, and HX3 varied within the range of 2.45–3.23. The HX2 samples had the highest Taylor factor of 3.23.

3.3. Hardness and wear resistance

As shown in Fig. 8, the hardness of the L-PBFed HX samples was evaluated. The lowest Vickers hardness value of 220.0 ± 2.2 HV was obtained from the HX1 sample. While the HX2 was the highest value of 239.2 ± 8.6 HV, and the HX3 was in between with a value of 231.2 ± 3.3 HV. The hardness tended to increase and then decrease when changing from HX1 to HX2 and then HX3, which is expected to relate to its wear performance.

After dry sliding pin-on-disk experiments, the widths of the wear track were observed using the SEM (Fig. 9), and the detailed values are summarized in Table 3. The wear track widths measured from the SEM images were 677.7 ± 18.6 μm (2 N), 1270.7 ± 23.1 μm (5 N), and 1901.1 ± 18.7 μm (10 N) for the HX1 sample. For the HX2 sample, these values were 732.3 ± 19.5 μm, 1116.6 ± 16.3 μm, and 1027.2 ± 12.2 μm, for 2 N, 5 N, and 10 N loads, respectively. The HX3 sample showed values of 851.3 ± 6.2 μm, 1505.1 ± 15.8 μm, and 1440.6 ± 11.3 μm for 2 N, 5 N, and 10 N loads, respectively. Under 2 N loading conditions, the lowest width values were observed in the HX1 samples, while increasing the load to 5 N or 10 N resulted in the lowest width values in the HX2 samples. In addition, the wear track exhibited a transition with increasing applied load. Abrasive wear was initially dominant at 2 N, followed by a mixed region of abrasive and adhesive wear at 5 N, and eventually smeared, adhered regions became predominant at 10 N.

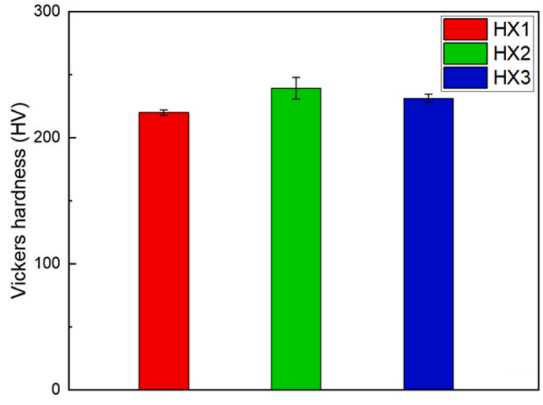

Fig. 8. Vickers hardness in the yz-plane of L-PBFed HX specimens.

Furthermore, mechanical profilometer analyses were performed to evaluate the depth of the wear tracks along with their widths. The profiles varied both beyond the sample groups and pin-on-disk loading conditions (Fig. 10). Under 2 N loading, the HX1 sample exhibited the smallest wear volume, whereas at 10 N, it showed the deepest wear track. The HX2 sample consistently demonstrated moderate wear depths across all conditions, representing the shallowest wear at 10 N. The HX3 sample showed the highest wear depths at 2 N and 5 N, and under 10 N loading, it displayed slightly lower wear depths compared to HX1.

Fig. 11 shows the plots of the coefficient of friction (CoF) for the L-PBFed HX samples, and the detailed values are summarized in Table 3. High fluctuation in CoF values was observed in all samples under the 2 N loading condition (Fig. 11(a)), which indicates unstable friction behavior. The average CoF value for HX1 was represented as 0.764, while HX2 showed a slightly lower value of 0.738. In contrast, HX3 exhibited a similar average CoF of 0.768 compared to HX1, it showed significantly higher fluctuations and deviation. Under a 5 N load, the fluctuation and deviations were lower and stabilized more quickly compared to the 2 N load in HX1 and HX2 (Fig. 11(b)), with the mean CoF values of 0.939 and 0.902, respectively. In addition, although HX3 showed the lowest CoF value of 0.877, it continued to exhibit relatively higher fluctuation and deviation compared to the other samples. At the highest load of 10 N, the fluctuation of CoF was reduced, and the difference in the mean CoF values between the samples became less pronounced (Fig. 11(c)). The average CoF values were 0.615 for HX1, 0.627 for HX2, and 0.625 for HX3, respectively. All samples reached steady-state CoF values at the early stage.

Additionally, EDS analysis revealed significant differences in oxide layer formation across the sample groups. As shown in Fig. 12(a−c), high oxygen content was observed on the surfaces under the 2 N loading condition, with atomic percentages ranging between 42.1% and 34.0%. However, when the load increased to 10 N (Fig. 12(d)), the oxygen content drastically decreased to 9.4%. Herein, only the results for the HX1 sample under the 10 N loading condition are shown to avoid presenting excessive data, this trend was consistent across all samples. This indicates that the oxidative wear mechanisms are predominantly activated under low loading conditions. On the other hand, the deformation wear mechanism manifests more distinctly under conditions of elevated loading. Particularly, the deep grooves were observed on the formed oxide layer (Fig. 12(d)).

3.4. Corrosion behavior

The comparative PDS curves of the L-PBFed HX samples are presented in Fig. 13. The key corrosion parameters, calculated from these curves, including corrosion potential (E_{corr}), corrosion current density (I_{corr}), critical pitting current density (I_{cc}), and polarization resistance (R_p), pitting potential (E_{pit}), are summarized in Table 4. The HX1 sample exhibited the highest E_{corr} of −105 mV, followed by HX2 at −116 mV, and HX3 at −130 mV. It can be noted that the reproducibility of the PDS curves, calculated based on the E_{corr} values, was determined as ± 16 mV, ± 5 mV, and ± 9 mV for the HX1, HX2, and HX3 samples, respectively. However, the differences in the measured E_{corr} values among the samples were within a small range and are considered experimentally insignificant.

On the other hand, all samples exhibited a passivation regime during polarization (Fig. 13). In this case, it should be considered that the alloys underwent localized corrosion. Therefore, to better compare the significant corrosion differences between the samples, it would be more meaningful to evaluate the I_{corr} values. The I_{corr} values of the specimens followed the trend HX2 < HX3 < HX1, indicating that HX2 had the

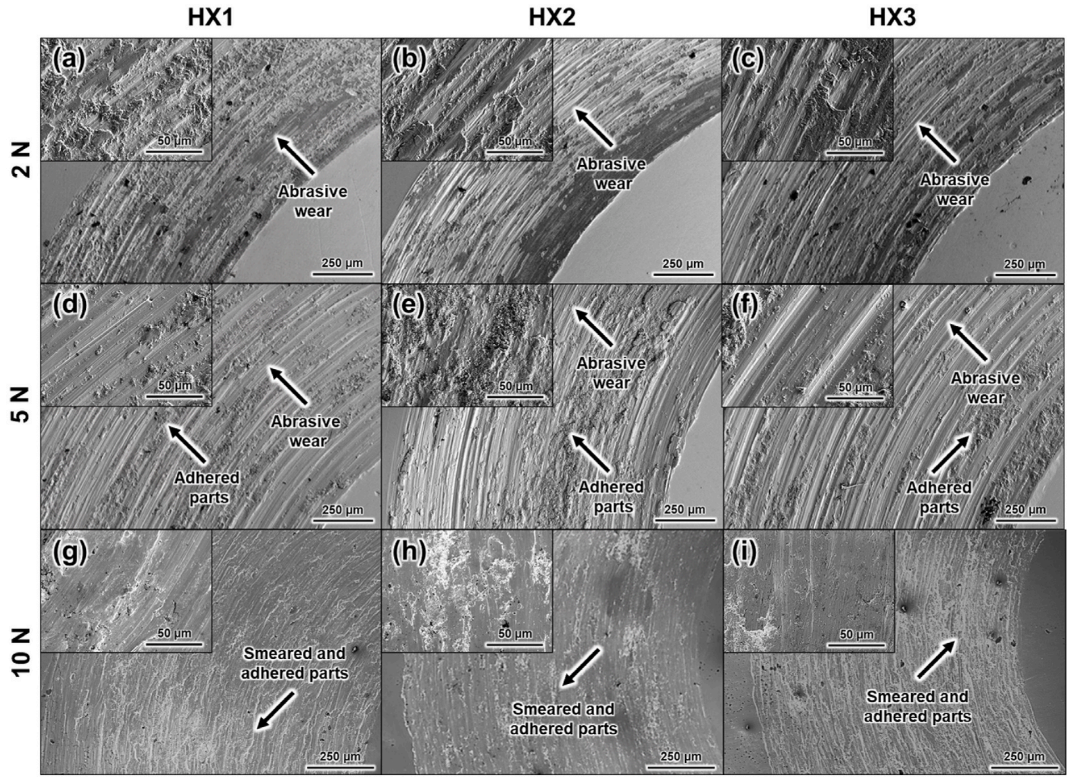

Fig. 9. Worn surface images of the HX1, HX2, and HX3 under increasing load conditions are shown. HX1, HX2, and HX3 were represented by (a, d, g), (b, e, h), and (c, f, i), respectively. The applied loads of 2 N, 5 N, and 10 N correspond to (a–c), (d–f), and (g–i).

Table 3
Wear track width based on SEM images and mean CoF values.

Sample	Wear Track Widths (μm)			CoF (mm^3/Nm)		
	2 N	5 N	10 N	2 N	5 N	10 N
HX1	677.7 ± 18.6 μm	1270.7 ± 23.1 μm	1901.1 ± 18.7 μm	0.764	0.939	0.615
HX2	732.3 ± 19.5 μm	1116.6 ± 16.3 μm	1027.2 ± 12.2 μm	0.738	0.902	0.627
HX3	851.3 ± 6.2 μm	1505.1 ± 15.8 μm	1440.6 ± 11.3 μm	0.768	0.877	0.625

lowest I_{corr} (26.63 μA/cm^2), followed by HX3 (33.13 μA/cm^2), with both being relatively close to each other. However, HX1 exhibited a significantly higher I_{corr}, approximately three times greater (84.71 μA/cm^2), suggesting a much higher corrosion rate. A similar trend was observed in the I_{cc} values, where HX1 displayed the highest critical current density, further supporting its lower corrosion resistance. The lower I_{corr} and I_{cc} values of HX2 and HX3 suggest better corrosion resistance and passivation behavior in the given environment compared to HX1. These findings are further supported by the polarization resistance (R_p) values, which align with the corrosion trends. HX2 displayed the highest R_p value of 305.57 Ω cm^2, indicating the formation of a more protective passive layer, whereas HX1 exhibited the lowest R_p (215.61 Ω cm^2), suggesting a weaker passive layer and a higher overall corrosion rate. Another critical parameter for locally corroded alloys is the pitting potential (E_{pit}). The E_{pit} values of all three samples were relatively close to each other. However, the HX3 sample exhibited a slightly nobler E_{pit} value compared to the other samples, indicating a slight improvement in resistance to localized corrosion.

4. Discussion

4.1. Influence of process parameters on densification and crystallographic texture

To understand the difference in the densification and crystallographic texture formation concerning the different VED inputs, the variations of melt pool in the yz-plane of the representative L-PBFed Hastelloy X samples were examined (Fig. 14). In the case of the HX1 sample, although the laser was scanned alternately in the x and y directions between layers, it was found that the comparatively larger melt

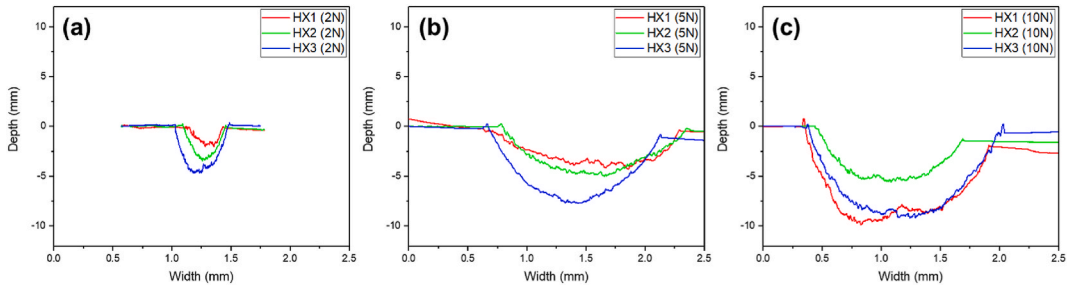

Fig. 10. Representative 2d profiles of wear debris of samples under varied wear loading conditions.

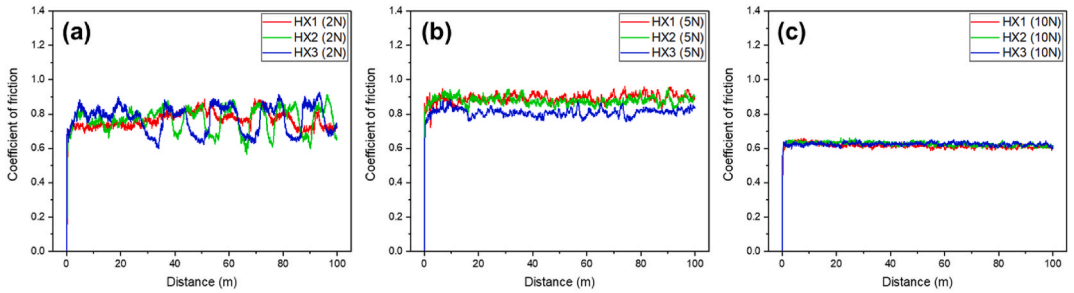

Fig. 11. CoF results of samples under varied wear loading conditions.

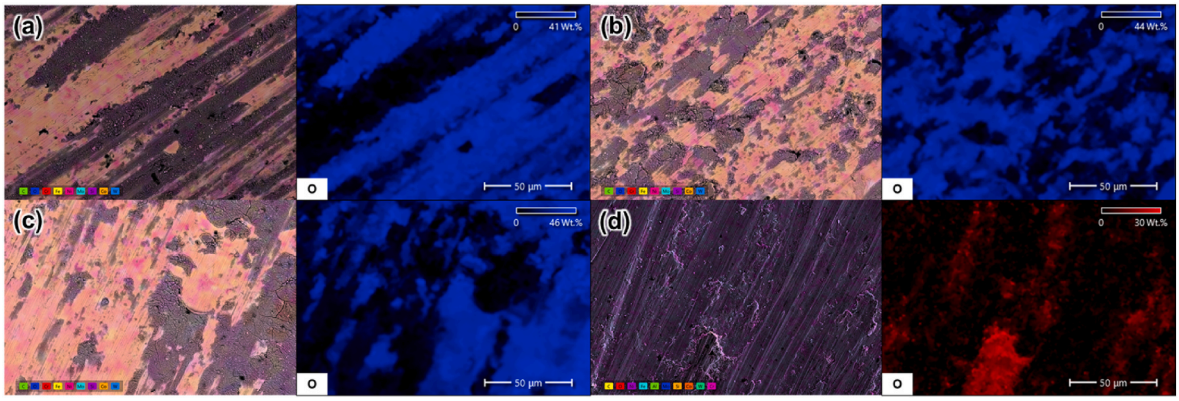

Fig. 12. SEM and corresponding EDS images of worn surfaces of (a) HX1, (b) HX2, and (c) HX3 specimens under the 2 N loading conditions. (d) Worn surface results of the HX1 specimen under a 10 N loading condition.

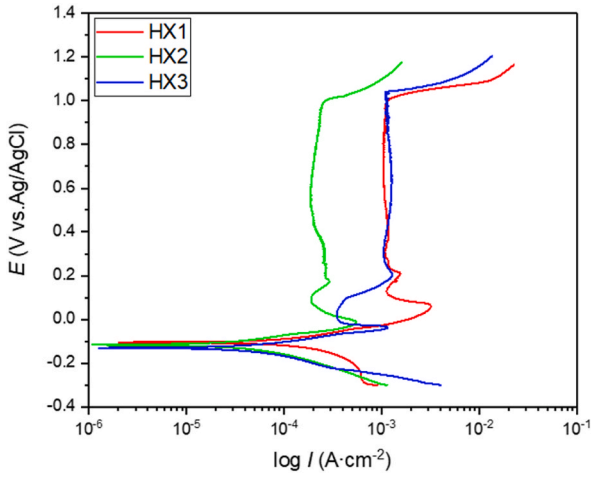

Fig. 13. The comparative PDS curves of L-PBFed HX samples in 3.5 wt% NaCl.

Table 4
Key corrosion parameters of L-PBFed Hastelloy-X samples calculated from the polarization curves.

Sample	E_{corr} (mV)	I_{corr} (μA·cm^{-2})	I_{cc} (μA·cm^{-2})	R_p (Ω·cm^2)	E_{pit} (mV)
HX1	−105	84.71	3.21 × 10^3	215.61	1019
HX2	−116	26.63	0.55 × 10^3	305.57	1001
HX3	−130	33.13	1.16 × 10^3	297.97	1043

pool size was attributed to the heightened VED resulting from slow *v* almost diminished the y direction laser scan melt pools, which was similar observation when applied to small powder bed thickness [42]. Meanwhile, in the HX2 and HX3 samples, the melt pool size gradually decreased with decreasing VED, and a y direction layer was also gradually visible. The melt pool size variation associated with the different VED inputs is closely related to the pore formation mechanisms during the L-PBF process, which are described in the previous studies [38,43,44]. As the surface temperatures approach the boiling point due to the laser radiation, the recoil pressure exerts an increasing force normal to the surface, resulting in the formation of a depression. After the decrease in temperature results is a decrease in the recoil force. Herein, the surface tension increases, overcoming the effects of the recoil force. Therefore, the direction of the melt flow velocity vector field is reversed towards the center. This reversal is abrupt and is due to the interaction between the recoil force and the surface tension (Marangoni effects), which generates the trapping of gas bubbles. Therefore, pores can be easily formed if the VED inputs are too high. However, a reduction in VED input has been demonstrated to be an effective method of decreasing recoil pressure and preventing the generation of pores in the samples [38,43], and the optimal VED input range for the high-densification sample fabrication was represented as 35−95 J/mm^3 [28], which includes the HX2 and HX3 samples in this study.

On the other hand, changes in VED are also an important factor for crystallographic texture development, because the variations in melt pool geometries induced by different VED inputs alter the growth direction of the cellular microstructures. As shown in Fig. 14, the observation of cell structures in the melt pool indicated the occurrence of cellular growth in all cases of examined samples owing to the high cooling rate of the L-PBF process [45,46], Furthermore, it has been established that the elongation direction of the cells coincides with <100> [47], which is the easy growth direction of face-centered cubic metals and the growth direction is perpendicular to the melt pool boundaries along the maximum temperature gradient direction [12,48]. Therefore, the developed crystallographic texture can be estimated from the preferred growth direction depending on the curvature of the melt pool boundaries. Similarly, it is deduced that the high VED input in the HX1 sample would have resulted in the formation of a narrow and deep

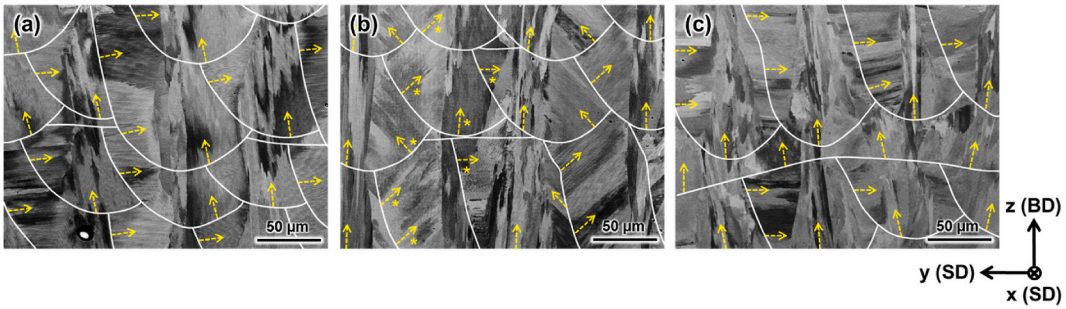

Fig. 14. SEM images of (a) HX1, (b) HX2, and (c) HX3 specimens in the yz-plane. The solid white lines show the melt pool traces, and the yellow arrows exhibit the direction of cell elongation. The * indicates the direction of cell growth rotated along the x and z directions.

melt pool that contributed to the cell elongation in two directions of 0° and 90° with respect to the z direction owing to the smaller curvature of the melt pool boundaries (Fig. 14(a)). Moreover, the sufficiently overlapped upper layer of melt pools prevents the sudden loss of epitaxial growth [23]. Therefore, the strong <100> alignments along the x,y, and z directions were manifested. On the other hand, the curvature of the melt pool boundaries was higher as the VED input decreased in the HX2 sample. Thus, cell growth on an incline to ± 45° along the z direction was observed at the side branching of melt pool boundaries, and 0° along the z direction was observed at the melt pool bottom, respectively. However, the direction was occasionally tilted to the x and z directions (indicated with *). Because the temperature gradient direction continuously changed with the rotation of the laser tracks between the deposited layers (Fig. 14(b)). Therefore, even though the epitaxial growth occurred across the layers, cell elongation with arbitrary orientation was exhibited, resulting in slightly deviated <100> and <110> components along the z direction. Thereafter, the HX3 sample once more represented the two cell elongation directions, 0° and 90° along the z-direction, with a decrease in curvature of the melt pool boundaries (Fig. 14(c)). In this instance, the induced 0° and 90° of cell elongation due to the comparatively smaller curvature of the melt pool boundaries promoted <100> alignments along the x,y, and z directions. Eventually, the crystallographic texture formation can be regulated by applying different VED inputs, which contribute to the morphology of the melt pool, and similar demonstrations can be found in L-PBFed other metals [26,49].

4.2. Effects of microstructural features on hardness and wear performance

The various VED inputs affect melt pool dynamics, resulting in densification and the associated crystallographic texture. This leads to different microstructural characteristics depending on the processing conditions, and these features will be important in determining surface performance, such as hardness and wear resistance. Initially, hardness was evaluated as it is a direct indicator of the underlying densification and microstructural characteristics and is strongly linked to tribological properties. As illustrated in Fig. 8, the hardness of L-PBFed HX samples initially increases from HX1 to HX2, followed by a decline in HX3 as the VED decreases. The lowest hardness in HX1 can be attributed to its low densification, which is likely caused by keyhole pores resulting from the excessive VED input. This is suggested that an optimal VED range maximizes hardness by promoting sufficient densification, which may have a more dominant influence on hardness than microstructural features under certain conditions. A similar observation has previously been reported [50,51], where increased densification led to higher hardness values due to reduced defects.

In addition to insufficient densification, the microstructural characteristics also explain the lowest hardness of the HX1 sample. The microstructure in the HX1 sample was characterized by the strongest crystallographic texture development, with a maximum MUD of 22.12. This was accompanied by a relatively large average grain size (34.57 μm) and the lowest average HAGBs distribution (23.14°) from epitaxial growth. The large grain size and the following lower HAGBs distribution contributed to the lower hardness, in accordance with the Hall-Petch relationship [52]. Moreover, low average KAM values (0.68°) and Taylor factor (2.45) further support the lowest hardness, reflecting a low level of dislocation density and resistance to plastic deformation, respectively.

In contrast, as the VED input decreased, both HX2 and HX3 achieved near full densification. Thus, their hardness is more closely associated with microstructural characteristics. Interestingly, the previously observed effects of the Hall-Petch relationship were not followed in this case. Consistent with a previous study [26], the reason can be considered that the stronger influence of crystallographic texture on the yield strength. As depicted in Fig. 6, HX2 exhibited a mixed crystallographic texture comprising both slightly tilted <100> and <110>, while HX3 was predominantly characterized by a <100> crystallographic texture. Although the theoretical Schmid factor for both <100> and <110> orientations is identical at 0.408, the actual deformation behaviour may differ due to different stress-transfer coefficients. The stress-transfer coefficients describe the ability of shear stress to be transferred across grain boundaries to neighboring grains [53]. Theoretically, A coefficient value close to 1 indicates easy transmission of slip, whereas a lower value implies increased resistance to slip transfer across the interfaces, thereby contributing to strengthening. From this perspective, HX2 can be considered as a low stress-transfer coefficient due to its mixed crystallographic texture, whereas HX3, with a nearly single <100> crystallographic texture, is likely to have a stress-transfer coefficient close to 1. These characteristics are further reflected in the highest Taylor factor values in HX2 (Fig. 7(d)), which indicate increased resistance to plastic deformation as a result of its prevailing crystallographic texture. Furthermore, HX2 exhibited a higher proportion of grain boundaries in the higher-angle range compared to HX3, which may further support strength through boundary-related mechanisms (Fig. 7(b)).

On the other hand, the tribological performance of the surface varied under different loading conditions. Surface topography, microstructural features, and mechanical properties are important parameters that determine the wear behavior [54,55]. During the 2 N loading condition, the HX1 sample exhibited the smallest wear width and depth, as observed by SEM and 2D profilometer, respectively. Under 5 N and 10 N loading conditions, the HX2 sample demonstrated the best performance. The variation in optimal wear performance depending on the applied load can be explained by a change in the dominant wear mechanism. Under the 2 N loading condition, oxidative wear was significant. Therefore, the formation of a rapid, uniform, and stable oxide film played a key role in enhancing wear resistance. According to previous literature [56], the oxidation rate of nickel is highest along the (100) crystallographic orientation. Thus, the strong <100> crystallographic texture of HX1 promoted the formation and adherence of a protective oxide layer during the wear test. This is further supported by SEM observation, which revealed that HX1 developed the most stable and

continuous oxide layer among the samples (Fig. 12(a–c)). However, as the applied load increased, hardness became the dominant factor influencing wear performance. As shown in Fig. 12(d), the breakdown of the oxide layer under high load conditions indicates a transition from oxidative wear to the activation of deformation wear mechanisms, similar to findings reported in Ref. [57]. In addition, the relatively low densification in the HX1 led to collapse and increased material removal, which accelerated wear. Under severe deformation conditions, the tribological response was closely aligned with hardness values, as also reported in previous studies [58,59]. Accordingly, HX2 with the highest hardness showed improved wear resistance under 5 N and 10 N loads, indicating the importance of the correlation between hardness and tribological performance in high-load conditions.

Furthermore, the fluctuation and deviation varied in the CoF results depending on the different applied VED (Fig. 11). Under the 2 N load, HX1 exhibited relatively stable and plateau friction behavior, whereas HX2 and HX3 showed periodic fluctuations. These differences in HX1 can be attributed to the formation of a continuous and adherent oxide layer, whereas in HX2 and HX3, cyclic formation and delamination of the oxide layers occurred during the friction, which is similar to the results reported in Ref. [57]. Therefore, the HX1 showed the best wear performance, even though it showed a relatively high mean CoF value in this condition. In contrast, HX3 experienced the most pronounced wear deterioration under the 5 N load, followed by HX1, whereas HX2 demonstrated the best wear resistance. This trend can also be inferred from the CoF behavior. Similar to the 2 N condition, HX3 displayed continued fluctuation and deviation in its CoF curve, suggesting that the cyclic formation and delamination of oxide layers have accelerated wear. On the other hand, although HX1 presented a more stable friction response, its wear performance deteriorated under the 5 N load due to the onset of additional deformation wear, as evidenced by the high CoF value. This may be attributed to structural collapse caused by its lower hardness, which is likely associated with its lower densification and strong crystallographic texture. At the highest load of 10 N, CoF plots for all samples became more stabilized. This stabilization is induced by high pin-on-disk load shifts the dominant wear mechanism from oxidation wear to deformation wear, thereby reducing the CoF deviation across all samples. This trend is also observed in the previous literature [60], indicating that mechanical properties such as hardness become increasingly important for wear resistance under high loads, and the CoF results also matched well with overall wear performance.

4.3. Corrosion response influenced by internal defects and microstructural features

It is well known that the corrosion resistance of LPBF-fabricated samples is primarily influenced by internal defects such as keyhole pores formed during fabrication, both on the surface and within the layers. These pores act as preferential sites for localized attack by aggressive ions, leading to localized acidification inside the pores. As a result, destabilizes the passive film and promotes pit initiation. Additionally, the diffusion of oxygen inside the pores is restricted, further hindering passivation and accelerating dissolution. In this study, the high relative density was observed in HX2 and HX3 samples, whereas HX1 contained more keyhole pores, as confirmed by OM images (Fig. 4). Post-corrosion SEM analysis revealed the presence of interlayer and internal porosities, with clear evidence of preferential corrosion around these defects.

In HX1, excessive volumetric energy density promoted keyhole-type pores that act as easy electrolyte pathways and hinder oxygen diffusion, which destabilizes the passive film and accelerates local acidification. Restricted oxygen ingress elevates the acidity inside the pores, resulting in locally higher solubility in these regions and increased surface conductivity. Consequently, it can be said that porosities act as preferential corrosion sites, and due to the insufficient oxygen supply, the corrosion process persists and accelerates in these regions.

It is well known that the corrosion susceptibility of a material can be evaluated from its E_{corr} values. However, this is generally valid for pure metals or alloys with highly stable passive films, since E_{corr} does not always provide a direct measure of corrosion resistance but rather reflects the thermodynamic tendency of the material to corrode. In contrast, for alloys that are capable of passivation yet prone to localized corrosion phenomena such as pitting, the I_{corr} is more reliable, as it is directly related to electrochemical reaction kinetics and thus provides a more realistic evaluation of the protective performance and corrosion resistance. Therefore, I_{corr} is particularly important for assessing long-term corrosion behavior by directly reflecting the stability of the passive film. For this reason, the comparative evaluation of the corrosion resistance of the HX alloys in this study was primarily based on I_{corr} values. Notably, HX1 exhibited a higher density of these corroded areas compared to HX2 and HX3 (Fig. 15). Furthermore, the HX1 sample displayed the highest I_{corr} and I_{cc} values, further supporting its lower corrosion resistance. Especially since higher I_{cc} values indicate greater susceptibility to active dissolution before passivation, this result suggests that pores disrupt the continuity of the passive film, making repassivation ineffective and allowing sustained corrosion attack [61]. It can be said that these combined effects significantly reduced the overall corrosion resistance of the HX1 alloy.

To further investigate characteristics of the passive film, SEM-EDS analysis was conducted around the corroded regions (Fig. 16). The elemental mapping results confirmed that Cr- and Mo-based oxides were primary protective phases, contributing to the formation of a stable passivation layer. In contrast, preferential dissolution of Ni and Fe was evident, as highlighted by the dashed regions, indicating their increased solubility in the corrosive environment. The accumulation of Ni and Fe around the corrosion pits suggests that these elements do not contribute to passivation. The passive film formed during anodic polarization is most likely composed of Cr_2O_3, Fe_2O_3, MoO_2, and MoO_3 in the HX [33]. This confirms that Cr and Mo play a key role in passivation stability, whereas defects around pits and pores, along with localized acidification, drive micro-galvanic effects, accelerating corrosion.

On the other hand, while minimizing defects helps prevent localized corrosion attack, corrosion behavior is also strongly influenced by the underlying microstructural characteristics. Previous studies on L-PBFed HX have shown that the passive film exhibits anisotropic behavior depending on the cross-sections, leading to differences in corrosion resistance [62,63]. This directional dependence is primarily attributed to variations in the underlying microstructure across different planes. One contributing factor is the grain refinement and the corresponding grain boundary density, which influence how readily passive films can nucleate. Another important factor is the distribution of dislocations. The higher dislocation density tends to facilitate passive film formation due to high local activation energy [63,64]. These results demonstrated that microstructural characteristics through different process parameters are critical for improving the corrosion performance of L-PBFed HX samples.

Interestingly, although both HX2 and HX3 exhibited high densification, HX2 showed better corrosion resistance. This is unexpected, as HX3 had finer grain sizes and higher KAM values, which are typically favorable for passivation. This difference may be attributed to crystallographic texture. In nickel-based alloys, the {100} orientation is more susceptible to pitting corrosion than the {110} and {111} orientations [65]. The {111} planes offer the highest resistance due to their low surface energy, high atomic packing density, which facilitates the formation of a more stable passive film [66]. Corrosion resistance has also been shown to follow the order {100} < {110} < {111}, owing to differences in passive film formation behavior [67]. In this study, HX3 exhibited predominantly <100> crystallographic texture, although the MUD values were lower than HX2. Whereas, HX2 represented the mixed crystallographic texture with contributions from both <100> and/or <110> orientations (Fig. 6). Therefore, it can be considered that grains with a dominant <100> orientation in HX3 may have been more

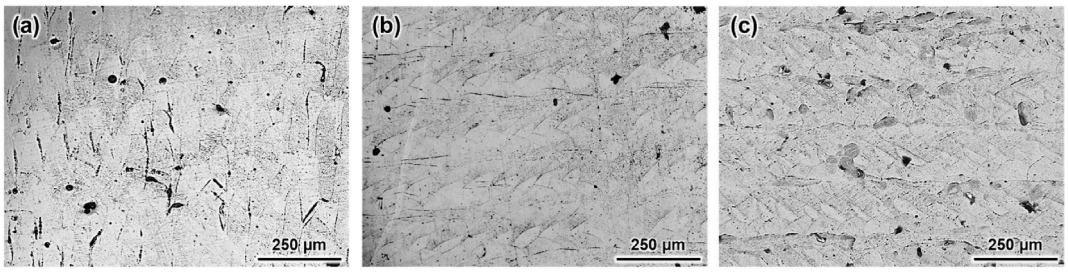

Fig. 15. SEM images of the L-PBFed Hastelloy-X samples after the corrosion tests in 3.5 wt% NaCl: (a) HX1, (b) HX2, and (c) HX3.

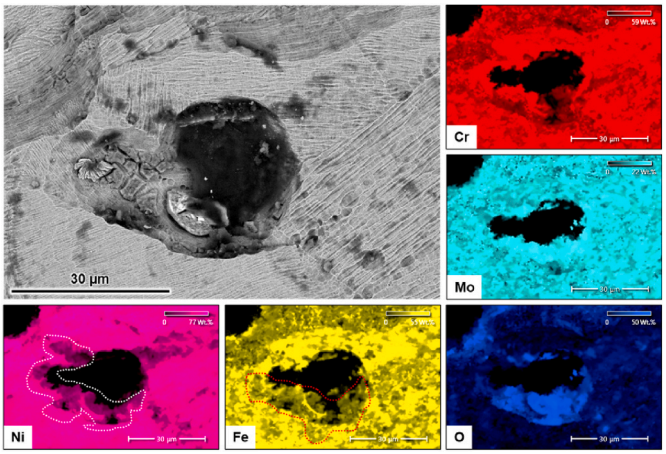

Fig. 16. Elemental mapping analysis of the corrosion pit formed on the HX1 alloy after corrosion test.

susceptible to corrosion due to less favorable passive film formation. Additionally, the relatively poor corrosion resistance observed in the HX1 sample, which exhibited the highest MUD value and thus the most pronounced crystallographic alignment, may hinder passive film formation compared to other conditions. Overall, these results indicate that crystallographic texture compromises the overall corrosion performance, even when other microstructural factors such as grain refinement and dislocation density appear beneficial in L-PBFed HX samples.

5. Conclusions

In this study, the effect of VED on the densification and microstructural evolution of HX components fabricated by the L-PBF process was systematically investigated. Based on the resulting microstructural characteristics, the corresponding tribological and corrosion performance were evaluated. According to the results obtained, the following conclusions can be drawn:

1. Different VED inputs resulted in distinct melt pool geometries, which influenced the densification of the fabricated samples. Excessive VED resulted in keyhole pores, resulting in relatively low densification. While proper VED input (35−95 J/mm^3) facilitated the optimized densification.
2. The variation in melt pool geometry induced by different VED altered the growth direction of <100> cellular microstructures. Therefore, distinct crystallographic texture evolutions were observed in each sample. HX1 showed strong <100> alignment in all directions, HX2 exhibited mixed <100> and <110> along the z direction, and HX3 represented weak <100> alignments throughout.
3. Hardness was found to be correlated with densification and crystallographic texture with followed by grain size, HAGBs, KAM, and Taylor factors. In addition, oxidative wear was dominant under low load (2 N) and influenced by surface oxide stability. Whereas, deformation wear became significant under higher load (10 N), where hardness played a more critical role in wear resistance.
4. Corrosion resistance showed that HX2 exhibited the lowest I_{corr} (26.63 μA/cm^2), followed closely by HX3 (33.13 μA/cm^2), indicating superior passivation. In contrast, HX1 had the highest I_{corr} values (84.71 μA/cm^2), approximately three times higher than HX2, suggesting weak passivation and higher dissolution rates. The differences can be associated with variation in densification and passive film formation behavior influenced by crystallographic texture.

These results highlight the critical role of process parameters in tailoring microstructural and functional properties of L-PBFed HX. Understanding the interplay between microstructural features and performance provides the concept for the design of wear and corrosion resistant components.

CRediT authorship contribution statement

Sung-Hyun Park: Formal analysis, Investigation, Visualization, Validation, Writing - Original Draft. **Fatmanur Ayten:** Formal analysis, Investigation. **Asli Gunay Bulutsuz:** Conceptualization, Methodology, Data curation, Supervision, Writing - Original Draft, Writing - Review & Editing. **Ozkan Gokcekaya:** Conceptualization, Methodology, Data curation, Supervision, Writing - Review & Editing. **Muhammed Enes İlgazi:** Formal analysis, Investigation. **Hakan Yilmazer:** Project administration, Writing - Review & Editing. **Burak Dikici:** Investigation, Writing - Original Draft, Writing - Review & Editing. **Takayoshi Nakano:** Conceptualization, Project administration, Funding acquisition, Writing - Review & Editing.

Declaration of competing interest

The authors declare that they have no known competing financial interests or personal relationships that could have appeared to influence the work reported in this paper.

Acknowledgments

This work was supported by the Japan Society for the Promotion of Science (JSPS) and CREST-Nanomechanics: Elucidation of macroscale mechanical properties based on understanding the nanoscale dynamics of innovative mechanical materials (Grant Number: JPMJCR2194) from the Japan Science and Technology Agency.

References

[1] Stopher MA. The effects of neutron radiation on nickel-based alloys. Mater Sci Technol 2017;33:518–36. https://doi.org/10.1080/02670836.2016.1187334.
[2] Akande IG, Oluwole OO, Fayomi OSI, Odunlami OA. Overview of mechanical, microstructural, oxidation properties and high-temperature applications of superalloys. Mater Today Proc 2021;43:2222–31. https://doi.org/10.1016/j.matpr.2020.12.523.
[3] Zhu J, Li D, Chang W, Wang Z, Hu L, Zhang Y, et al. In situ marine exposure study on corrosion behaviors of five alloys in coastal waters of western Pacific Ocean.

J Mater Res Technol 2020;9:8104–16. https://doi.org/10.1016/j.jmrt.2020.05.060.
[4] Reed RC, Tao T, Warnken N. Alloys-by-design: application to nickel-based single crystal superalloys. Acta Mater 2009;57:5898–913. https://doi.org/10.1016/j.actamat.2009.08.018.
[5] Zhao J-C, Larsen M, Ravikumar V. Phase precipitation and time-temperature-transformation diagram of Hastelloy X. Mater Sci Eng, A 2000;293:112–9. https://doi.org/10.1016/S0921-5093(00)01049-2.
[6] Sakthivel T, Laha K, Nandagopal M, Chandravathi KS, Parameswaran P, Panneer Selvi S, et al. Effect of temperature and strain rate on serrated flow behaviour of Hastelloy X. Mater Sci Eng, A 2012;534:580–7. https://doi.org/10.1016/j.msea.2011.12.011.
[7] Shindo M, Kondo T. Evaporation behavior of Hastelloy-X alloys in simulated very high temperature reactor environments. Nucl Technol 1984;66:429–38. https://doi.org/10.13182/NT84-A33445.
[8] Eren Z, Gokcekaya O, Balkan D, Nakano T, Mecitoğlu Z. Comparison of in-plane compression of additively manufactured Ti6Al4V 2D auxetic structures: lattice design, manufacturing speed, and failure mode. Mater Des 2024;241. https://doi.org/10.1016/j.matdes.2024.112885.
[9] Kim YS, Gokcekaya O, Sato K, Ozasa R, Matsugaki A, Nakano T. In-situ alloying of nonequiatomic TiNbMoTaW refractory bio-high entropy alloy via laser powder bed fusion: achieving suppressed microsegregation and texture formation. Mater Des 2025;252. https://doi.org/10.1016/j.matdes.2025.113824.
[10] Frazier WE. Metal additive manufacturing: a review. J Mater Eng Perform 2014;23:1917–28. https://doi.org/10.1007/s11665-014-0958-z.
[11] Sun SH, Hagihara K, Ishimoto T, Suganuma R, Xue YF, Nakano T. Comparison of microstructure, crystallographic texture, and mechanical properties in Ti–15Mo–5Zr–3Al alloys fabricated via electron and laser beam powder bed fusion technologies. Addit Manuf 2021;47. https://doi.org/10.1016/j.addma.2021.102329.
[12] Ishimoto T, Morita N, Ozasa R, Matsugaki A, Gokcekaya O, Higashino S, et al. Superimpositional design of crystallographic textures and macroscopic shapes via metal additive manufacturing—Game-change in component design. Acta Mater 2025;286. https://doi.org/10.1016/j.actamat.2025.120709.
[13] Dan C, Cui Y, Wu Y, Chen Z, Liu H, Ji G, et al. Achieving ultrahigh fatigue resistance in AlSi10Mg alloy by additive manufacturing. Nat Mater 2023;22:1182–8. https://doi.org/10.1038/s41563-023-01651-9.
[14] Lin D, Hu J, Liu M, Li Z, Xi X, Dai J, et al. Enhancing plasticity in laser additive manufactured high-entropy alloys: the combined effect of thermal cycle induced dissolution and twinning. Addit Manuf 2024;93. https://doi.org/10.1016/j.addma.2024.104427.
[15] Liu Y, Zhang J, Tan Q, Yin Y, Liu S, Li M, et al. Additive manufacturing of high strength copper alloy with heterogeneous grain structure through laser powder bed fusion. Acta Mater 2021;220. https://doi.org/10.1016/j.actamat.2021.117311.
[16] Park SH, Gokcekaya O, Oh MH, Nakano T. Effects of hatch spacing on densification, microstructural and mechanical properties of β-solidifying γ-TiAl alloy fabricated by laser powder bed fusion. Mater Char 2024;214. https://doi.org/10.1016/j.matchar.2024.114077.
[17] Xi X, Lin D, He Z, Ma R, Wei H, Shi Z, et al. Additively manufactured crack-free nickel-based superalloy with synergistic strength and plasticity via grain refinement and striped oxides inhibition. Compos Pt B-Eng 2025;291. https://doi.org/10.1016/j.compositesb.2024.112038.
[18] Iveković A, Montero-Sistiaga ML, Vleugels J, Kruth J-P, Vanmeensel K. Crack mitigation in laser powder bed fusion processed Hastelloy X using a combined numerical-experimental approach. J Alloys Compd 2021;864:158803. https://doi.org/10.1016/j.jallcom.2021.158803.
[19] Han Q, Gu Y, Setchi R, Lacan F, Johnston R, Evans SL, et al. Additive manufacturing of high-strength crack-free Ni-based Hastelloy X superalloy. Addit Manuf 2019;30. https://doi.org/10.1016/j.addma.2019.100919.
[20] Agrawal S, Avadhani GS, Suwas S. Effect of heat treatments on laser powder bed fusion processed Hastelloy X: insights into the deformation mechanism. Mater Sci Eng, A 2025;923. https://doi.org/10.1016/j.msea.2024.147662.
[21] Yin Y, Zhang J, Pan S, Xing Y, Yue X, Chang W. Room- and elevated-temperature mechanical property of selective laser melting-fabricated Hastelloy X with different heat treatments. Mater Sci Eng, A 2023;886. https://doi.org/10.1016/j.msea.2023.145697.
[22] Bahl S, Mishra S, Yazar KU, Kola IR, Chatterjee K, Suwas S. Non-equilibrium microstructure, crystallographic texture and morphological texture synergistically result in unusual mechanical properties of 3D printed 316L stainless steel. Addit Manuf 2019;28:65–77. https://doi.org/10.1016/j.addma.2019.04.016.
[23] Biswas P, Ma J. Development of crystallographic misorientation in laser powder bed fusion 316L stainless steel. Addit Manuf 2024;80. https://doi.org/10.1016/j.addma.2023.103951.
[24] Nadammal N, Mishurova T, Fritsch T, Serrano-Munoz I, Kromm A, Haberland C, et al. Critical role of scan strategies on the development of microstructure, texture, and residual stresses during laser powder bed fusion additive manufacturing. Addit Manuf 2021;38. https://doi.org/10.1016/j.addma.2020.101792.
[25] Chen J, Liu Z, Liu C, Zhang B, Liu T, Chen G, et al. Effects of scanning strategy and scanning speed on microstructures and mechanical properties of NiTi alloys by laser powder bed fusion. Mater Sci Eng, A 2024;914. https://doi.org/10.1016/j.msea.2024.147115.
[26] Gokcekaya O, Ishimoto T, Hibino S, Yasutomi J, Narushima T, Nakano T. Unique crystallographic texture formation in Inconel 718 by laser powder bed fusion and its effect on mechanical anisotropy. Acta Mater 2021;212. https://doi.org/10.1016/j.actamat.2021.116876.
[27] Park SH, Gokcekaya O, Nitomakida T, Nakano T. Effects of heat accumulation strategies on defects and microstructure of pure chromium fabricated by laser powder bed fusion: an experimental and numerical study. J Mater Res Technol 2024;33:7333–44. https://doi.org/10.1016/j.jmrt.2024.11.049.
[28] Hibino S, Todo T, Ishimoto T, Gokcekaya O, Koizumi Y, Igashira K, et al. Control of crystallographic texture and mechanical properties of hastelloy-X via laser powder bed fusion. Crystals 2021;11. https://doi.org/10.3390/cryst11091064.
[29] Sanchez-Mata O, Wang X, Muñiz-Lerma JA, Atabay SE, Attarian Shandiz M, Brochu M. Dependence of mechanical properties on crystallographic orientation in nickel-based superalloy Hastelloy X fabricated by laser powder bed fusion. J Alloys Compd 2021;865:158868. https://doi.org/10.1016/j.jallcom.2021.158868.
[30] Sanchez-Mata O, Wang X, Muñiz-Lerma JA, Atabay SE, Attarian Shandiz M, Brochu M. Characterization of the microstructure and mechanical properties of highly textured and single crystal Hastelloy X thin struts fabricated by laser powder bed fusion. J Alloys Compd 2022;901. https://doi.org/10.1016/j.jallcom.2021.163465.
[31] Keshavarzkermani A, Esmaeilizadeh R, Ali U, Enrique PD, Mahmoodkhani Y, Zhou NY, et al. Controlling mechanical properties of additively manufactured hastelloy X by altering solidification pattern during laser powder-bed fusion. Mater Sci Eng, A 2019;762. https://doi.org/10.1016/j.msea.2019.138081.
[32] Zhang S, Shi Y, Zhang Y, Guo P, Li X, Luo K. Electrochemical anisotropy of Hastelloy X fabricated by selective laser melting in a NaNO3 solution. J Alloys Compd 2023;951. https://doi.org/10.1016/j.jallcom.2023.169947.
[33] Chaudry UM, Han SC, Tayyab K bin, Farooq A, Kim WS, Jun TS. Unraveling the anisotropic corrosion behavior along the building direction in laser powder bed fusion processed Hastelloy X. J Mater Res Technol 2024;33:1188–200. https://doi.org/10.1016/j.jmrt.2024.09.115.
[34] Trisnanto SR, Wang X, Brochu M, Omanovic S. Effects of crystallographic orientation on the corrosion behavior of stainless steel 316L manufactured by laser powder bed fusion. Corros Sci 2022;196. https://doi.org/10.1016/j.corsci.2021.110009.
[35] Yousif MAS, Al-Deheish IA, Ali U, Akhtar SS, Al-Athel KS. Mechanical, tribological, and corrosion behavior of laser powder-bed fusion 316L stainless steel parts: effect of build orientation. J Mater Res Technol 2024;33:1220–33. https://doi.org/10.1016/j.jmrt.2024.09.105.
[36] Ishimoto T, Hagihara K, Hisamoto K, Sun S-H, Nakano T. Crystallographic texture control of beta-type Ti–15Mo–5Zr–3Al alloy by selective laser melting for the development of novel implants with a biocompatible low Young's modulus. Scr Mater 2017;132:34–8. https://doi.org/10.1016/j.scriptamat.2016.12.038.
[37] Guo C, Li S, Shi S, Li X, Hu X, Zhu Q, et al. Effect of processing parameters on surface roughness, porosity and cracking of as-built IN738LC parts fabricated by laser powder bed fusion. J Mater Process Technol 2020;285. https://doi.org/10.1016/j.jmatprotec.2020.116788.
[38] Luo X, Yang C, Fu ZQ, Liu LH, Lu HZ, Ma HW, et al. Achieving ultrahigh-strength in beta-type titanium alloy by controlling the melt pool mode in selective laser melting. Mater Sci Eng, A 2021;823. https://doi.org/10.1016/j.msea.2021.141731.
[39] Jalali A, Nikniazi A, Gholamzadeh H, Yin S, Malekan M, Ahn SY, et al. Hot-cracking mitigation and microcrack formation mechanisms in laser powder bed fusion processed hastelloy X and cantor high entropy alloys. Met Mater Int 2024. https://doi.org/10.1007/s12540-024-01711-y.
[40] Sadowski M, Ladani L, Brindley W, Romano J. Optimizing quality of additively manufactured Inconel 718 using powder bed laser melting process. Addit Manuf 2016;11:60–70. https://doi.org/10.1016/j.addma.2016.03.006.
[41] Zhang X, Xu H, Li Z, Dong A, Du D, Lei L, et al. Effect of the scanning strategy on microstructure and mechanical anisotropy of Hastelloy X superalloy produced by laser powder bed fusion. Mater Char 2021;173. https://doi.org/10.1016/j.matchar.2021.110951.
[42] Amano H, Ishimoto T, Hagihara K, Suganuma R, Aiba K, Sun SH, et al. Impact of gas flow direction on the crystallographic texture evolution in laser beam powder bed fusion. Virtual Phys Prototyp 2023;18. https://doi.org/10.1080/17452759.2023.2169172.
[43] Hojjatzadeh SMH, Parab ND, Guo Q, Qu M, Xiong L, Zhao C, et al. Direct observation of pore formation mechanisms during LPBF additive manufacturing process and high energy density laser welding. Int J Mach Tool Manufact 2020;153. https://doi.org/10.1016/j.ijmachtools.2020.103555.
[44] Khairallah SA, Anderson AT, Rubenchik A, King WE. Laser powder-bed fusion additive manufacturing: physics of complex melt flow and formation mechanisms of pores, spatter, and denudation zones. Acta Mater 2016;108:36–45. https://doi.org/10.1016/j.actamat.2016.02.014.
[45] Wang H, Wang L, Cui R, Wang B, Luo L, Su Y. Differences in microstructure and nano-hardness of selective laser melted Inconel 718 single tracks under various melting modes of molten pool. J Mater Res Technol 2020;9:10401–10. https://doi.org/10.1016/j.jmrt.2020.07.029.
[46] Park SH, Gokcekaya O, Ozasa R, Oh MH, Kim YW, Kim HS, et al. Microstructure and crystallographic texture evolution of β-Solidifying γ-TiAl alloy during single- and multi-track exposure via laser powder bed fusion. Met Mater Int 2024;30:1227–41. https://doi.org/10.1007/s12540-023-01579-4.
[47] Karthik GM, Kim ES, Zargaran A, Sathiyamoorthi P, Jeong SG, Kim HS. Role of cellular structure on deformation twinning and hetero-deformation induced strengthening of laser powder-bed fusion processed CuSn alloy. Addit Manuf 2022;54. https://doi.org/10.1016/j.addma.2022.102744.
[48] Wan HY, Zhou ZJ, Li CP, Chen GF, Zhang GP. Effect of scanning strategy on grain structure and crystallographic texture of Inconel 718 processed by selective laser melting. J Mater Sci Technol 2018;34:1799–804. https://doi.org/10.1016/j.jmst.2018.02.002.

[49] Luo X, Song T, Gebert A, Neufeld K, Kaban I, Ma H, et al. Programming crystallographic orientation in additive-manufactured beta-type titanium alloy. Adv Sci 2023;10. https://doi.org/10.1002/advs.202302884.
[50] Cherry JA, Davies HM, Mehmood S, Lavery NP, Brown SGR, Sienz J. Investigation into the effect of process parameters on microstructural and physical properties of 316L stainless steel parts by selective laser melting. Int J Adv Manuf Technol 2015; 76:869–79. https://doi.org/10.1007/s00170-014-6297-2.
[51] Liu K, Gu D, Guo M, Sun J. Effects of processing parameters on densification behavior, microstructure evolution and mechanical properties of W–Ti alloy fabricated by laser powder bed fusion. Mater Sci Eng, A 2022;829. https://doi.org/10.1016/j.msea.2021.142177.
[52] Hansen N. Hall-petch relation and boundary strengthening. Scr Mater 2004;51: 801–6. https://doi.org/10.1016/j.scriptamat.2004.06.002.
[53] Livingstont JD, Chalmers B. Multiple slip in bicrystal deformation. Acta Metall Mater 1957;5:322–7. https://doi.org/10.1016/0001-6160(57)90044-5.
[54] Bulutsuz AG, Gulec B, Gokcekaya O, Gardstam J, Nakano T, Yilmazer H. An investigation over microstructure and HIP processing effects on wear performance of pure chromium parts fabricated by laser powder bed fusion. Int J Refract Metals Hard Mater 2024;120. https://doi.org/10.1016/j.ijrmhm.2024.106616.
[55] Orgeldinger C, Seynstahl A, Rosnitschek T, Tremmel S. Surface properties and tribological behavior of additively manufactured components: a systematic review. Lubricants 2023;11. https://doi.org/10.3390/lubricants11060257.
[56] Bonfrisco LP, Frary M. Effects of crystallographic orientation on the early stages of oxidation in nickel and chromium. J Mater Sci 2010;45:1663–71. https://doi.org/10.1007/s10853-009-4144-x.
[57] Zong H, Kang N, El Mansori M. Impact of applied loads on wear mechanisms in H13 steel at various preheating temperatures during laser powder bed fusion additive manufacturing. Wear 2024:556–7. https://doi.org/10.1016/j.wear.2024.205538.
[58] Hu J, Lin X, Hu Y. High wear resistance and strength of Hastelloy X reinforced with TiC fabricated by laser powder bed fusion additive manufacturing. Appl Surf Sci 2024;648. https://doi.org/10.1016/j.apsusc.2023.159004.
[59] Kumar S, Chakraborty M, Subramanya Sarma V, Murty BS. Tensile and wear behaviour of in situ Al-7Si/TiB2 particulate composites. Wear 2008;265:134–42. https://doi.org/10.1016/j.wear.2007.09.007.
[60] Nanjundaiah RS, Rao SS, Praveenkumar K, Prabhu TR, Shettigar AK, Patel GCM, et al. Fretting wear behavior on LPBF processed AlSi10Mg alloy for different heat treatment conditions. J Mater Res Technol 2024;30:4330–46. https://doi.org/10.1016/j.jmrt.2024.04.147.
[61] Singh VB, Gupta A. Active, passive and transpassive dissolution of In-718 alloy in acidic solutions. Mater Chem Phys 2004;85:12–9. https://doi.org/10.1016/j.matchemphys.2003.11.025.
[62] Yin Y, Zhang J, Huo J, Zhao K, Zhu X, Meng X, et al. Effect of microstructure on the passive behavior of selective laser melting-fabricated Hastelloy X in NaNO3 solution. Mater Char 2020;165. https://doi.org/10.1016/j.matchar.2020.110370.
[63] Yin Y, Li H, Pan S, Zhang J, Han Q, Yang S. Electrochemical behaviour of passivation film formed on SLM-fabricated Hastelloy X superalloy surface in 10 wt % NaNO3 solution. Corros Sci 2022;206. https://doi.org/10.1016/j.corsci.2022.110494.
[64] Yin Y, Zhang J, Yang S, Liu T, Han Q, Zhang Z, et al. Effect of microstructure on the electrochemical dissolution behaviour of Hastelloy® X superalloy processed by selective laser melting and heat treatments. Mater Des 2021;206. https://doi.org/10.1016/j.matdes.2021.109828.
[65] Zhang LN, Szpunar JA, Dong JX, Ojo OA, Wang X. Dependence of crystallographic orientation on pitting corrosion behavior of ni-fe-cr alloy 028. Metall Mater Trans B 2018;49:919–25. https://doi.org/10.1007/s11663-018-1227-6.
[66] Zhao T, Wang R, Zhang HF, Zhang CH, Zhang S, Chen HT, et al. An investigation on the effect of heat input to wear behavior and corrosion-cavitation erosion mechanism of Hastelloy C-276 coating by cold metal transfer. Mater Char 2024; 210. https://doi.org/10.1016/j.matchar.2024.113819.
[67] Gray JJ, El Dasher BS, Orme CA. Competitive effects of metal dissolution and passivation modulated by surface structure: an AFM and EBSD study of the corrosion of alloy 22. Surf Sci 2006;600:2488–94. https://doi.org/10.1016/j.susc.2006.04.002.